

# Compositionally complex doping for zero-strain zero-cobalt layered cathodes

<https://doi.org/10.1038/s41586-022-05115-z>

Received: 23 September 2021

Accepted: 14 July 2022

Published online: 21 September 2022

 Check for updates

Rui Zhang<sup>1,9</sup>, Chunyang Wang<sup>1,9</sup>, Peichao Zou<sup>1</sup>, Ruqian Lin<sup>2</sup>, Lu Ma<sup>3</sup>, Liang Yin<sup>4</sup>, Tianyi Li<sup>4</sup>, Wenqian Xu<sup>4</sup>, Hao Jia<sup>5</sup>, Qiuyan Li<sup>5</sup>, Sami Sainio<sup>6</sup>, Kim Kisslinger<sup>7</sup>, Stephen E. Trask<sup>8</sup>, Steven N. Ehrlich<sup>3</sup>, Yang Yang<sup>3</sup>, Andrew M. Kiss<sup>3</sup>, Mingyuan Ge<sup>3</sup>, Bryant J. Polzin<sup>8</sup>, Sang Jun Lee<sup>6</sup>, Wu Xu<sup>5</sup>, Yang Ren<sup>4</sup> & Huolin L. Xin<sup>1,✉</sup>

The high volatility of the price of cobalt and the geopolitical limitations of cobalt mining have made the elimination of Co a pressing need for the automotive industry<sup>1</sup>. Owing to their high energy density and low-cost advantages, high-Ni and low-Co or Co-free (zero-Co) layered cathodes have become the most promising cathodes for next-generation lithium-ion batteries<sup>2,3</sup>. However, current high-Ni cathode materials, without exception, suffer severely from their intrinsic thermal and chemo-mechanical instabilities and insufficient cycle life. Here, by using a new compositionally complex (high-entropy) doping strategy, we successfully fabricate a high-Ni, zero-Co layered cathode that has extremely high thermal and cycling stability. Combining X-ray diffraction, transmission electron microscopy and nanotomography, we find that the cathode exhibits nearly zero volumetric change over a wide electrochemical window, resulting in greatly reduced lattice defects and local strain-induced cracks. In-situ heating experiments reveal that the thermal stability of the new cathode is significantly improved, reaching the level of the ultra-stable NMC-532. Owing to the considerably increased thermal stability and the zero volumetric change, it exhibits greatly improved capacity retention. This work, by resolving the long-standing safety and stability concerns for high-Ni, zero-Co cathode materials, offers a commercially viable cathode for safe, long-life lithium-ion batteries and a universal strategy for suppressing strain and phase transformation in intercalation electrodes.

Lithium-ion batteries (LIBs) are the ubiquitous power supplier in portable electronics, power tools and a growing proportion of the global light- and medium-duty automobile fleet. In particular, in pursuit of global greenhouse gas emission reduction goals, high-energy-density LIBs play an increasingly critical role<sup>4–7</sup>. Cobalt (Co), a key component for stabilizing the cathodes, has been widely introduced in today's ternary high-Ni  $\text{LiNi}_{1-x-y}\text{Mn}_x\text{Co}_y\text{O}_2$  (NMC) and  $\text{LiNi}_{1-x-y}\text{Co}_x\text{Al}_y\text{O}_2$  (NCA) systems to suppress the Li/Ni cation mixing and enhance their thermal stability<sup>8–10</sup>. However, owing to its lower abundance and to geopolitical issues, Co is considered the highest material supply chain risk for electric vehicles in the short and medium term. The economic, security and societal drivers lead to a growing consensus in the battery community of the need to lessen and/or eliminate Co in cathode materials without sacrificing their performance<sup>11</sup>. Moreover, although Co is widely considered to boost the rate performance<sup>12</sup>, some recent research has reported that Co is even more destructive than Ni because of the chemo-mechanical cracking and irreversible oxygen release at high voltage<sup>13,14</sup>. In this context, developing high-Ni, zero-Co cathodes has attracted great attention and a variety of promising strategies, such as bulk doping and surface passivation, have been developed<sup>15–18</sup>.

Despite the fact that some of the zero-Co cathodes reported have delivered a comparable capacity and cycling performance compared with Co-reliant cathodes, the intrinsic thermal and chemo-mechanical instabilities<sup>19–21</sup> of high-Ni cathodes remain a catastrophic safety issue that hinders their commercialization and practical applications. In particular, the large volume change that ubiquitously exists in high-Ni cathode materials could cause both structural degradations and mechanical failures. On the one hand, the large lattice contraction along the  $c$  axis unavoidably results in detrimental O1 stacking faults or phase and thereby the deactivation of high-Ni cathodes<sup>20</sup>. On the other hand, local strain concentration originating from heterogeneous volume change could directly cause mechanical failure of the cathodes through the formation of multiscale cracks (including both intergranular cracking and intragranular cracking)<sup>9,22</sup>. Another universal drawback is that nearly all of the high-Ni cathodes, irrespective of Co level, suffer from intrinsically poor thermal tolerance in the delithiated state, owing to the strong oxidizability of  $\text{Ni}^{4+}$  and oxygen release<sup>23,24</sup>. The detrimental cracking and highly reactive surface synergistically exacerbate the thermal instability, leading to thermal run-away and even explosion. It is concluded that one thing all current high-Ni cathodes share is the

<sup>1</sup>Department of Physics and Astronomy, University of California, Irvine, CA, USA. <sup>2</sup>Chemistry Division, Brookhaven National Laboratory, Upton, NY, USA. <sup>3</sup>National Synchrotron Light Source II, Brookhaven National Laboratory, Upton, NY, USA. <sup>4</sup>X-ray Science Division, Argonne National Laboratory, Lemont, IL, USA. <sup>5</sup>Energy and Environment Directorate, Pacific Northwest National Laboratory, Richland, WA, USA. <sup>6</sup>Stanford Synchrotron Radiation Lightsource, SLAC National Accelerator Laboratory, Menlo Park, CA, USA. <sup>7</sup>Center for Functional Nanomaterials, Brookhaven National Laboratory, Upton, NY, USA. <sup>8</sup>Chemical Sciences and Engineering Division, Argonne National Laboratory, Lemont, IL, USA. <sup>9</sup>These authors contributed equally: Rui Zhang, Chunyang Wang. <sup>✉</sup>e-mail: huolin.xin@uci.edu

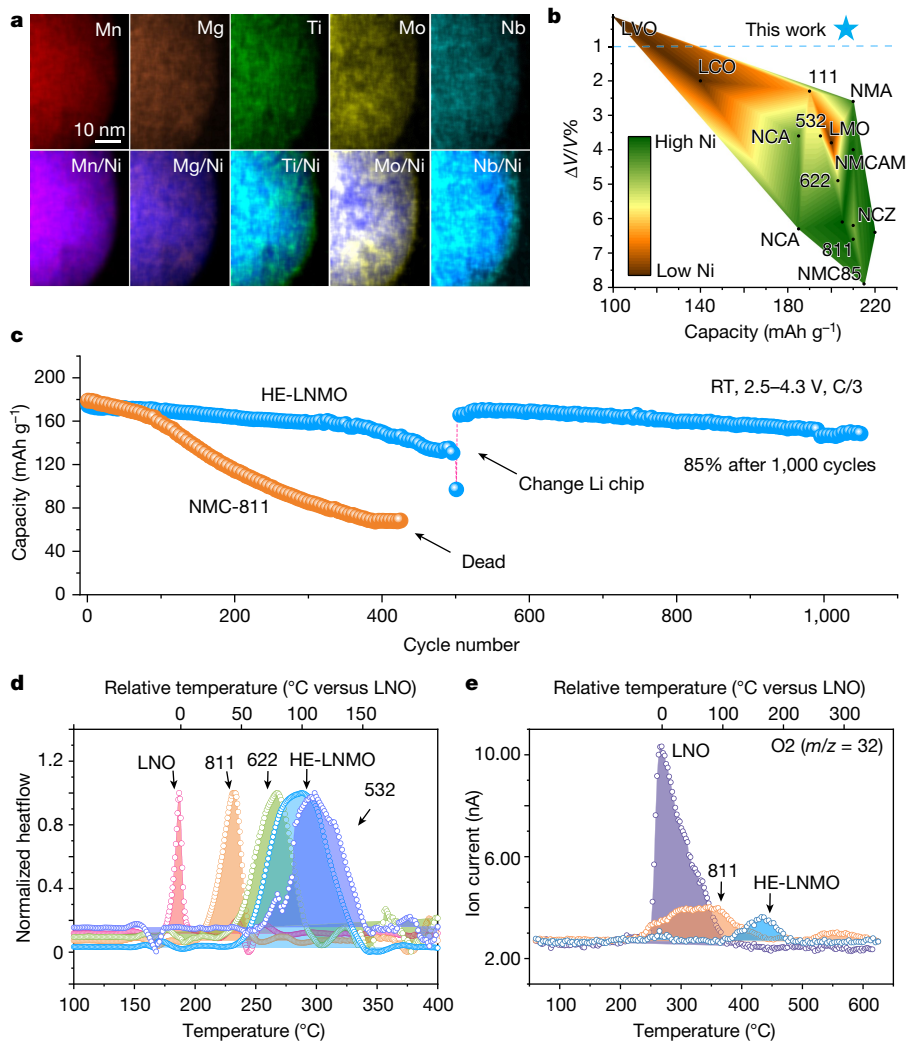


**Fig. 1 | Superior stability of the HE-LNMO cathode.** **a**, EDS maps of the doping elements and their maps overlapped with Ni. **b**, Volumetric change versus capacity for the HE-LNMO and other cathode materials with different Ni contents. **c**, Cycle life of the half cells containing HE-LNMO and NMC-811 at C/3

with cutoff voltage 2.5–4.3 V (versus Li/Li<sup>+</sup>). **d**, DSC profile of delithiated LiNiO<sub>2</sub> (LNO), NMC-811, NMC-622, HE-LNMO and NMC-532. **e**, TGA-MS of LNO, NMC-811 and HE-LNMO. The high oxygen-loss temperature and low oxygen intensity confirm the superior thermal stability of HE-LNMO.

trade-off between capacity and stability. Therefore, we propose that the key to resolving the long-standing stability and safety challenges facing the current high-Ni, zero-Co cathodes is to break the trade-off by mitigating the structural degradation and reducing the volume change without sacrificing their high capacity during operation. Unfortunately, the current doping and coating technologies still fall short in solving the stability–capacity trade-off dilemma.

High-entropy materials are an emerging class of new materials that consist of multiple components. Through the combination of multiple principal elements, the configurational entropy can be maximized and robust properties can be achieved<sup>25</sup>. Stimulated by the concept of entropy stabilization in metallic alloys, the strategy has been rapidly extended to oxide systems for energy storage<sup>26,27</sup>. However, because high-Ni content provides the only route for high-energy-density cathodes, the conventional near-equimolar strategy has been proven unfeasible<sup>28</sup>. Inspired by the conventional high-entropy stabilization strategies, in this work we propose the concept of compositionally complex (high-entropy) doping to resolve the long-standing stability–capacity dilemma of high-Ni cathodes. A zero-strain zero-Co layered cathode, LiNi<sub>0.8</sub>Mn<sub>0.13</sub>Ti<sub>0.02</sub>Mg<sub>0.02</sub>Nb<sub>0.01</sub>Mo<sub>0.02</sub>O<sub>2</sub> (HE-LNMO, where HE denotes high-entropy doped, L is Li, N is Ni, M is Mn, Ti, Mg, Mo, Nb, and O is oxygen), is developed by using this new doping

strategy with a typical co-precipitation method (see Methods). Energy-dispersive spectroscopy (EDS) mappings (Fig. 1a) show that all the transition metals in the high-entropy-doped cathode, HE-LNMO, distribute homogeneously in the particle interior. Ti, Mo and Nb are slightly enriched on the primary particle's surface. EDS quantification (Supplementary Fig. 2) suggests that the dopants' atomic ratios are consistent with the designed formula of LiNi<sub>0.8</sub>Mn<sub>0.13</sub>Ti<sub>0.02</sub>Mg<sub>0.02</sub>Nb<sub>0.01</sub>Mo<sub>0.02</sub>O<sub>2</sub>. Compared with most of the cutting-edge high-Ni and low-Co cathodes, HE-LNMO exhibits an unprecedented zero volumetric change (Fig. 1b and Extended Data Table 1) during Li<sup>+</sup> intercalation and deintercalation, realizing zero strain and high capacity simultaneously. Benefiting from the highly stable structure, HE-LNMO shows significantly improved capacity retention (85% at 1,000 cycles in a half cell) compared with commercial LiNi<sub>0.8</sub>Mn<sub>0.1</sub>Co<sub>0.1</sub>O<sub>2</sub> (NMC-811) (Fig. 1c). Meanwhile, HE-LNMO exhibits superior thermal stability comparable to LiNi<sub>0.5</sub>Mn<sub>0.3</sub>Co<sub>0.2</sub>O<sub>2</sub> (NMC-532), which has a much lower Ni content (Fig. 1d,e). The superior structural stability can be attributed to the following aspects: (1) mitigated oxygen loss due to the pinning effects from the dopants; (2) reduced lattice expansion and contraction and defect generation; (3) suppressed cation mixing and rock-salt transformation through multicomponent dopants. By resolving the stability and safety concerns facing

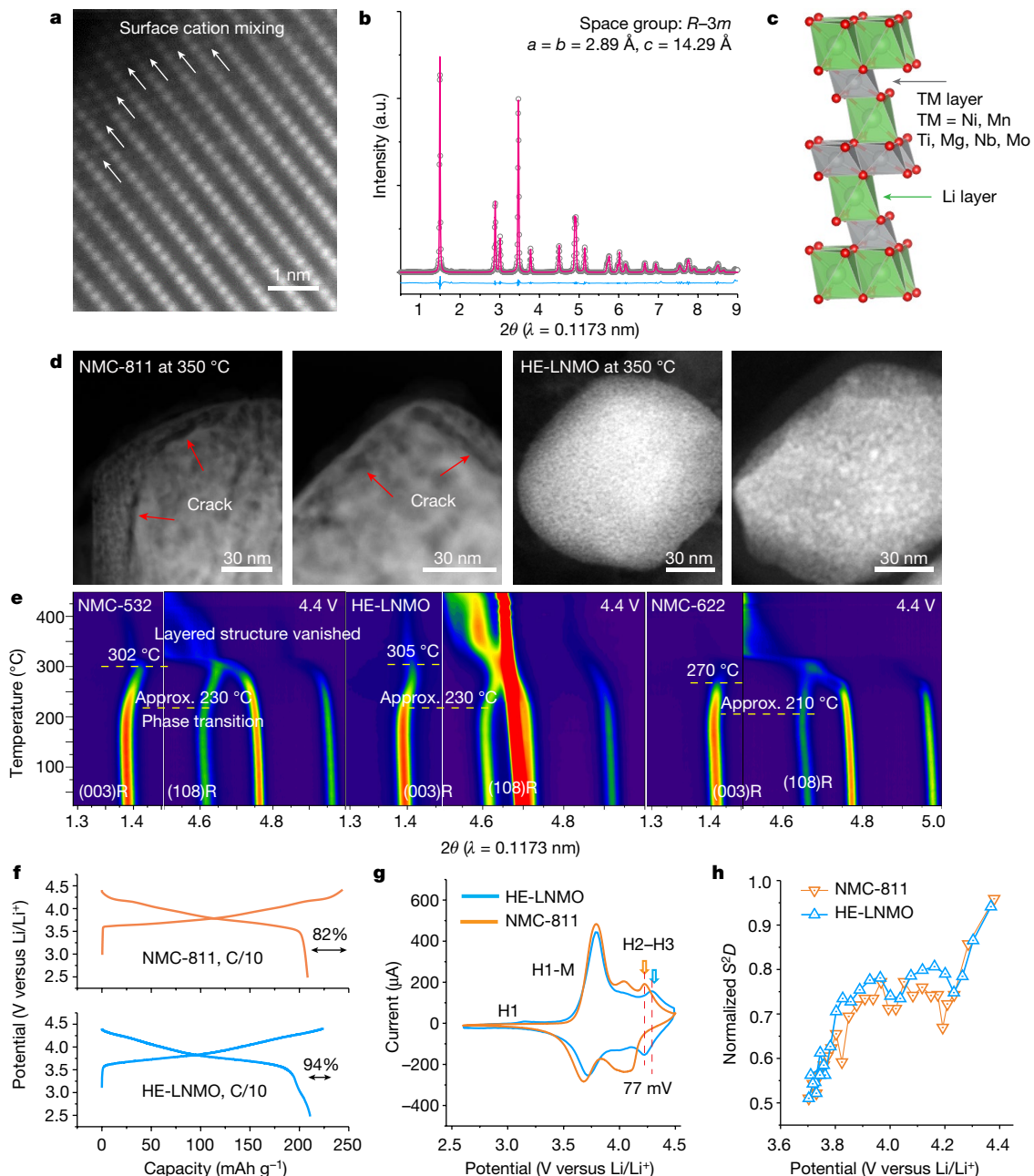


**Fig. 2 | Structural and electrochemical characterizations of HE-LNMO layered cathode.** **a**, A representative atomic-resolution HAADF-STEM image of a pristine HE-LNMO primary particle. **b**, The XRD pattern and the fitting curve of HE-LNMO. **c**, An atomic model of HE-LNMO with an O<sub>3</sub> lattice. **d**, Representative HAADF-STEM images of delithiated NMC-811 (left) and HE-LNMO (right) after in-situ heating. **e**, Synchrotron-based XRD of the delithiated cathode during in-situ heating. **f**, The initial charge–discharge profiles and Columbic efficiencies of NMC-811 and HE-LNMO. **g**, The second-cycle CV of HE-LNMO and NMC-811 in half cells. **h**, The Li<sup>+</sup> diffusion constant of HE-LNMO and NMC-811 at 30 °C obtained by the GITT. approx., approximately.

current high-Ni cathodes, this work provides a promising solution to the commercialization and deployment of zero-Co cathodes in next-generation LIBs.

### Cathode material characterization

High-angle annular dark-field scanning transmission electron microscopy (HAADF-STEM) image (Fig. 2a) shows that the pristine HE-LNMO has a well-defined layered structure with only a slight Li–Ni mixing at the particle’s surface, similar to that in previously reported high-Ni cathode materials<sup>29</sup>. Statistical synchrotron-based powder X-ray diffraction (XRD) and refinement (Fig. 2b) confirm that HE-LNMO has a space group

of *R*-3*m* with the lattice parameters of  $a = b = 2.89 \text{ \AA}$ , and  $c = 14.29 \text{ \AA}$ , which are slightly higher than that of NMC-811 (additional structural characterization is available in the Supplementary Information Figs. 1–4). The atomic model of HE-LNMO is illustrated in Fig. 2c, in which the transition metals, Li and O locate at the 3*b*, 3*a* and 6*c* sites, respectively.

### Thermal stability

Suffering from extremely poor thermal stability, Ni-rich cathodes exhibit serious safety issues, especially at high states of charge. In-situ heating experiments in (scanning) transmission electron microscopes (S)TEMs (Fig. 2d and Extended Data Fig. 1a, b) show that severe

nanocracks form in delithiated NMC-811 primary particles after being heated to 350 °C, whereas only tiny voids are observed in delithiated HE-LNMO under the same conditions. EDS analysis (Extended Data Fig. 1c) shows that the dopant distribution in HE-LNMO after thermal abuse remains nearly unchanged, indicating outstanding thermal stability. Synchrotron-based *in-situ* heating XRD is used to track the phase transformation pathway of the delithiated HE-LNMO compared with commercial LiNi<sub>0.6</sub>Mn<sub>0.2</sub>Co<sub>0.2</sub>O<sub>2</sub> (NMC-622) and NMC-532 under harsh thermal conditions. Fig. 2e shows that the layer-structured HE-LNMO starts to transform into a spinel structure at 230 °C and then completely into rock salt at 305 °C, comparable to that of commercial NMC-532 and far better than that of NMC-622 and NMC-811 (ref.<sup>30</sup>). Normalized differential scanning calorimetry (DSC) profiles of a series of conventional Ni-rich cathodes (Fig. 1d) show that their thermal stability generally decreases with increasing Ni content. Yet, as an exception, the HE-LNMO, which has the same Ni content (80%) as that of NMC-811, delivers a notable peak temperature at 286 °C, which is approaching the 292 °C of NMC-532. The enthalpy quantification (Extended Data Fig. 2a) of the exothermic peak of HE-LNMO is 530.0 J g<sup>-1</sup>, which is much lower than that of NMC-811 (983.9 J g<sup>-1</sup>). Thermogravimetric analysis–mass spectrometer (TGA–MS) results (Fig. 1e) further validate the superior oxygen retention of HE-LNMO in the charged state, whereby the maximum oxygen release temperature of HE-LNMO is delayed by approximately 100 °C compared with that of NMC-811.

## Electrochemical performance

Electrochemical tests were performed to evaluate the performance of HE-LNMO in comparison with NMC-811. The charge–discharge profiles (Fig. 2f) show that HE-LNMO delivers an initial discharge capacity of 210.1 mAh g<sup>-1</sup>, which is comparable to that of NMC-811 (208.2 mAh g<sup>-1</sup>), and the initial Coulombic efficiency of HE-LNMO reaches 94%, which is significantly improved compared with the 82% of NMC-811. The detrimental H2–H3 transition in HE-LNMO is also significantly suppressed as indicated by the flattened plateau at around 4.25 V. Cyclic voltammetry (CV) (Fig. 2g) shows that, compared with NMC-811, the M–H2 redox peak in HE-LNMO is considerably flattened, and its H2–H3 redox peak shifts towards a higher potential by 77 mV, suggesting the multistep phase transitions are considerably ‘postponed’ in HE-LNMO. In addition, the reduced polarization difference from the reversible H1–M phase transition in HE-LNMO is smaller than that of NMC-811, indicating more favourable reversibility and higher Li<sup>+</sup> diffusion dynamics in HE-LNMO, which are also confirmed by the galvanostatic intermittent titration technique (GITT) in Fig. 2h and electrochemical impedance spectroscopy (EIS) results (Extended Data Fig. 2b). Figures 3a–e and 1c show the long-term cycling performances of HE-LNMO in both half cells and full cells at room temperature. HE-LNMO shows remarkable capacity retention at different cutoff voltages, for example, 98.5% capacity retention after 100 cycles at 2.5–4.4 V (versus Li/Li<sup>+</sup>) and 98% capacity retention after 50 cycles at 2.5–4.5 V (versus Li/Li<sup>+</sup>). In sharp contrast, NMC-811 shows only 87.1% and 85.8% capacity retention, respectively, after the same cycling. In single-layer pouch cell tests (Fig. 3d,e), HE-LNMO shows excellent cycling performances with capacity retention of higher than 95% at 2.8–4.2 V (versus graphite) after 500 cycles, comparable to that of current-state-of-the-art high-Ni cathodes<sup>31</sup>. High-temperature cycling at 50 °C shows that commercial NMC-811 has a rapid capacity degradation with 90.3% after 50 cycles, whereas HE-LNMO shows significantly enhanced capacity retention (96.6% after 50 cycles) at the same temperature, demonstrating superior stability and suppressed side reactions at high temperatures (Extended Data Fig. 3).

## Structural stability

Figure 3f,g shows the X-ray absorption near edge structure (XANES) of Ni in HE-LNMO and NMC-811 after 100 cycles. The Ni-K edge of cycled

HE-LNMO nearly overlaps with that of the pristine sample; by contrast, the Ni-K edge in cycled NMC-811 shifts to higher energy, suggesting some of the interior volumes of NMC-811 cannot be fully reduced, probably because Li<sup>+</sup> diffusion is impeded owing to the surface rock salt built-up<sup>32</sup>. Fourier-transformed extended X-ray absorption fine structures (FT-EXAFS) of the Ni-K and Mn-K edges (Fig. 3h,i and Extended Data Fig. 4) show that both the (Ni, Mn)–O and (Ni, Mn)–transition metal (TM) coordination distances in NMC-811 are noticeably shortened after long-term cycling, indicating lattice shrinkage and generation of defects. However, these interatomic peak shifts are almost negligible in cycled HE-LNMO, suggesting highly stable local coordination environments. XANES of other transition metals (Fig. 3j–m) show that the Mn edge in long-cycled HE-LNMO overlaps well with that of the pristine sample, whereas for the Ti, Nb and Mo a slight edge difference is observed after cycling, indicating that oxygen vacancies are probably confined around these high-valence dopants owing to the ‘pinning effect’, which thereby leads to mitigated oxygen loss around Ni redox centres. This pinning effect is further evidenced by the FT-EXAFS of transition metals (Extended Data Fig. 4a–c). The major transition metals—Ni and Mn—have the same TM–O bonding length, whereas for those high-valence dopants, the TM–O bonding length is remarkably shorter than Ni–O or Mn–O bonding, suggesting that oxygen atoms are dragged towards these elements. The dopant–oxygen bonding shows slight shifts after cycling (Extended Data Fig. 4d), confirming that the oxygen vacancies or defects are ‘trapped’ around these dopants, stopping the formation of crack embryos through the aggregation of vacancies<sup>19</sup>. This structural stability is also evidenced by multidimensional characterizations (Extended Data Fig. 5). Wavelet-transformed EXAFS shows that, compared with that in HE-LNMO, the Ni–O bonding in NMC-811 is extended along the high-*k* direction, suggesting more oxygen-related defects in NMC-811. The soft X-ray absorption of the Ni-L3 edge shows that, compared with NMC-811, HE-LNMO has a higher Ni-L3<sub>high</sub> proportion in the TEY mode, suggesting that HE-LNMO has better charge–discharge homogeneity and less surface reconstruction compared with NMC-811 (ref.<sup>33</sup>). Electron diffractions of the pristine and long-term cycled cathode show that the cycled HE-LNMO maintains a perfect O<sub>3</sub> structure similar to that in the pristine particles; XRD measurements show that the lattice change of long-term cycled HE-LNMO is extremely small compared with that of NMC-811; EDS analysis of the cycled HE-LNMO shows similar elemental distributions as that of pristine particles; meanwhile, X-ray fluorescence quantification shows considerably reduced transition metal ion dissolution on the graphite anode compared with NMC-811. All of these results confirm the superior cycling stability of HE-LNMO.

Synchrotron-based XRD is applied to quantify the lattice change during a single charge–discharge cycle. The lattice parameters (Fig. 4a) and volume variation (Fig. 4b) at different cutoff voltages during delithiation are calculated on the basis of the XRD data (Fig. 4c,d). The results show that, for HE-LNMO, the maximum changes of the *a* and *c* axes are as low as –0.5% and 0.9%, respectively. Meanwhile, for NMC-811, the corresponding values are –1.9% and 2.1%, respectively, which are more than double that of HE-LNMO. Furthermore, the maximum volume changes (cutoff 4.3 V) of HE-LNMO and NMC-811 are determined to be approximately –0.3% and –2.7%, respectively (Fig. 4b). That is to say, the volume change of HE-LNMO is nearly an order of magnitude smaller than that of the NMC-811, reaching beyond the ‘zero strain’ state (volume change < 1%)<sup>34</sup>. *In-situ* delithiation experiments in TEM are performed on HE-LNMO and the parental phase of high-Ni cathodes—LiNiO<sub>2</sub>. Strain analyses (Fig. 4e) of the *in-situ* delithiated particles show that HE-LNMO remains nearly defect free and strain free during delithiation; by contrast, large amounts of dislocations are formed in delithiated LiNiO<sub>2</sub>. The suppression of the defect generation significantly reduced the local strain concentration inside primary particles and thereby validates the robust structural stability of HE-LNMO. Furthermore, the structural stability of HE-LNMO

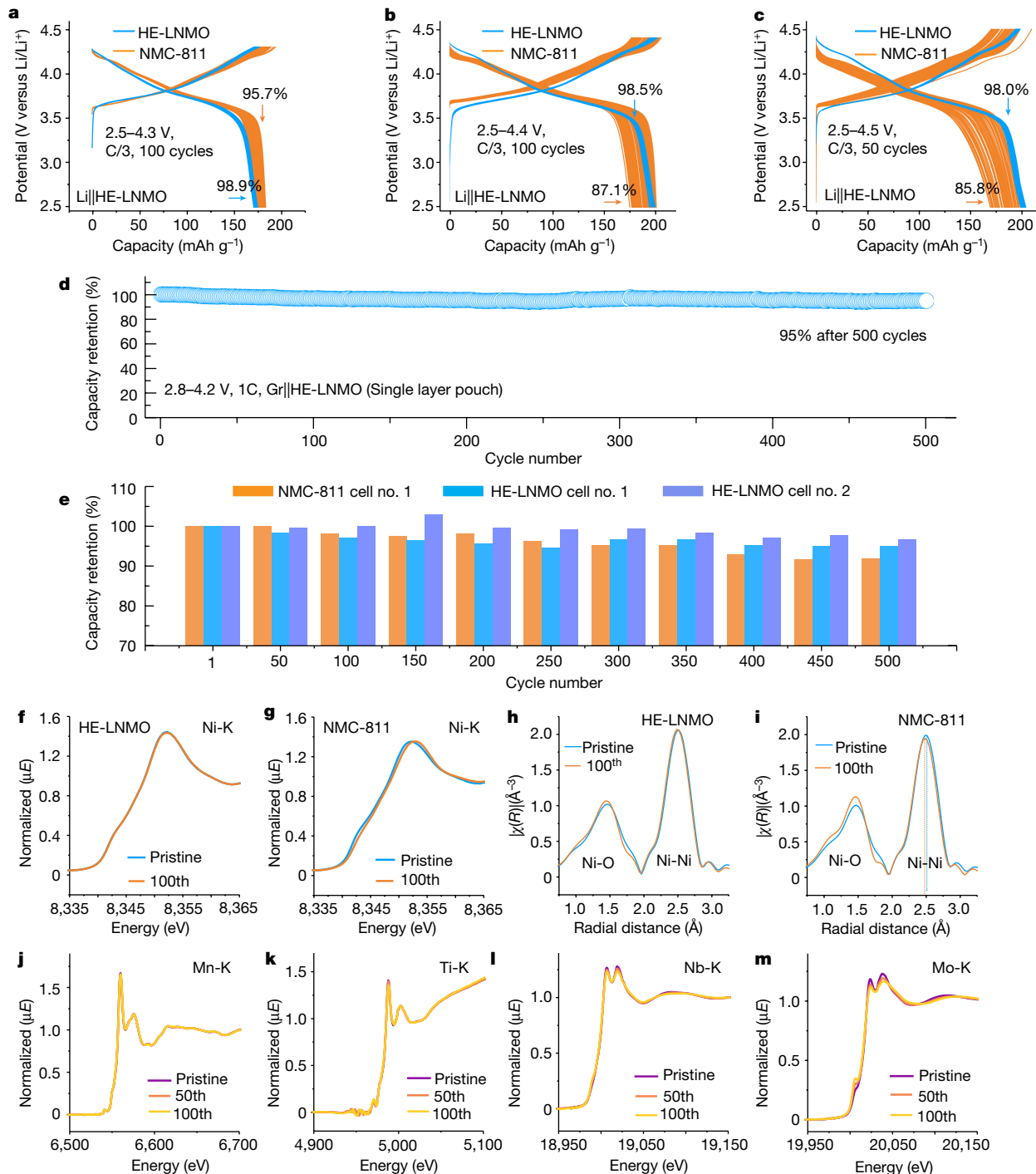


**Fig. 3 | Cycling stability and local coordinate environment stability of HE-LNMO.** **a–c**, Long-cycle charge–discharge profiles of the half cells containing HE-LNMO and NMC-811, within 2.5–4.3 V (versus Li/Li<sup>+</sup>) (**a**), 2.5–4.4 V (versus Li/Li<sup>+</sup>) (**b**) and 2.5–4.5 V (versus Li/Li<sup>+</sup>) (**c**) at the current of C/3, respectively. **d,e**, Long-term cycling capacity retentions of HE-LNMO (**d**) and NMC-811 (**e**) in a

pouch cell using graphite (Gr) as an anode with a cutoff voltage 2.8–4.2 V. **f,g**, The Ni-K edge XANES spectrum of pristine and cycled HE-LNMO (**f**) and NMC-811 (**g**). **h,i**, FT-EXAFS of pristine and cycled HE-LNMO (**h**) and NMC-811 (**i**). **j–m**, XANES of Mn-K (**j**), Ti-K (**k**), Nb-K (**l**) and Mo-K (**m**) edges of HE-LNMO after different cycles.

was evaluated by transmission X-ray microscope (TXM) tomography and scanning electron microscopy (SEM) cross-section analyses at the secondary-particle level. Figure 4f shows the three-dimensional (3D) reconstructions of representative long-term-cycled NMC-811 and HE-LNMO secondary particles. Substantial intergranular cracks (indicated by the arrows) formed inside NMC-811, whereas no obvious cracks are observed in HE-LNMO. The above results demonstrate that the unique pinning effect suppresses both lattice deformation

(for example, dislocation nucleation and slips) and nano/microcrack generation during long-term cycling.

## Generality and transferrability

To demonstrate that the compositionally complex doping strategy has generality, we further synthesized and investigated a series of layered cathodes with different Ni contents and different dopants. These

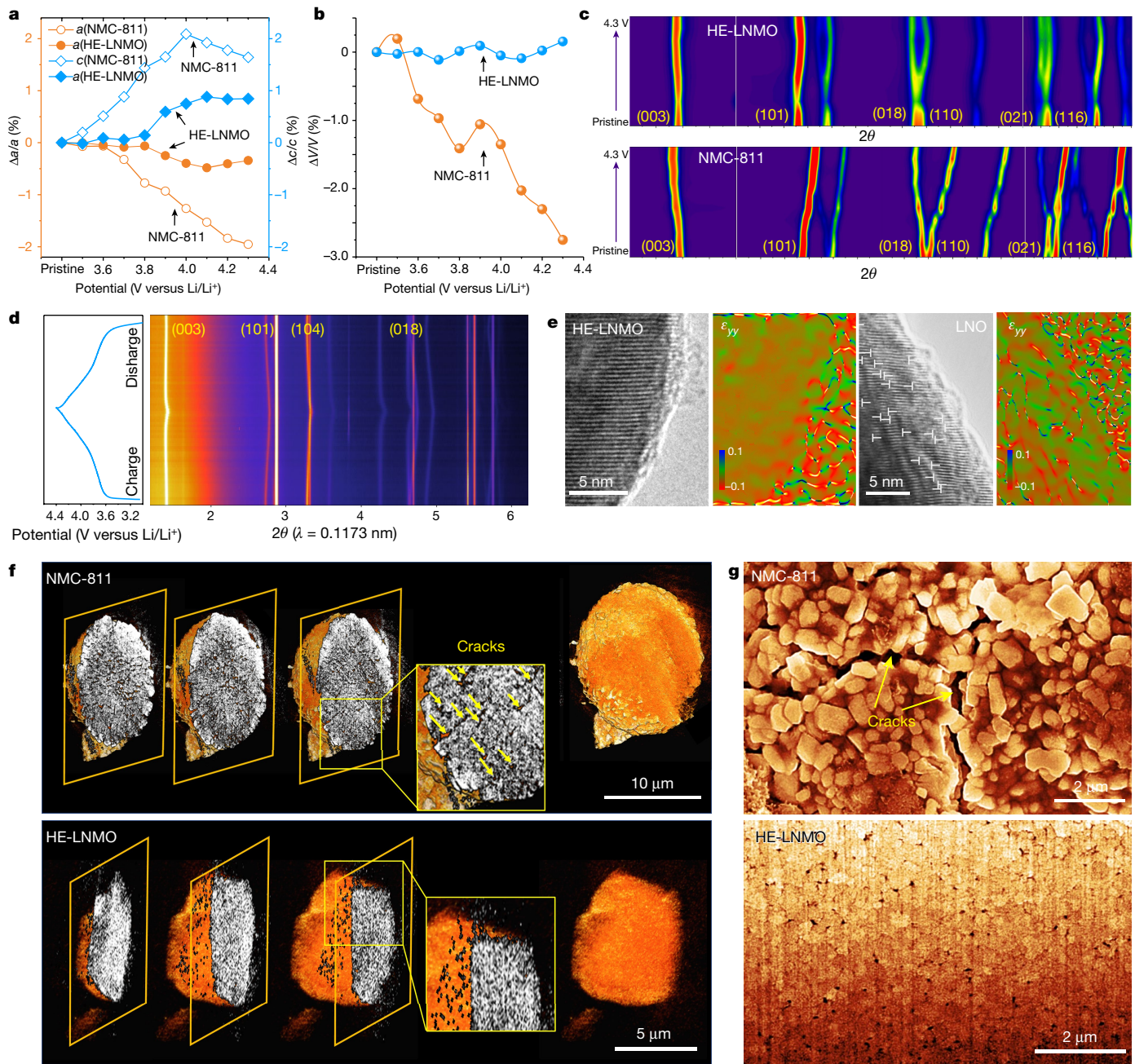


**Fig. 4 | Structural and mechanical stability of HE-LNMO.** **a, b**, Lattice parameter ( $a$  and  $c$  axes) and volume change of HE-LNMO in comparison with NMC-811 during the first charge, within 3.0–4.3 V (versus Li/Li<sup>+</sup>). **c**, Ex-situ XRD patterns of HE-LNMO in comparison with NMC-811. **d**, Synchrotron-based in-situ XRD patterns of HE-LNMO during charge and discharge. **e**, Strain state of the in-situ delithiated HE-LNMO and LNO obtained by geometrical phase analysis (GPA). Substantial dislocations are identified in the delithiated LNO.

**f**, Synchrotron-based TXM tomography showing the 3D structure of the NMC-811 and HE-LNMO secondary particles after long-term cycling (100 cycles, 2.5–4.4 V (versus Li/Li<sup>+</sup>), 1C). Substantial cracks (indicated by the arrows) are identified in cycled NMC-811 (upper panel), whereas no evident cracks are observed in HE-LNMO (lower panel). **g**, Representative SEM cross-section images of NMC-811 (upper panel) and HE-LNMO (lower panel) secondary particles.

results can be found in the Supplementary Information, Figs. 10–19. For instance, HE-Ni90 with the composition of  $\text{LiNi}_{0.9}\text{Mn}_{0.03}\text{Ti}_{0.02}\text{Mg}_{0.02}\text{Mo}_{0.02}\text{Nb}_{0.01}\text{O}_2$ , HE-N70 with the composition of  $\text{LiNi}_{0.7}\text{Mn}_{0.23}\text{Ti}_{0.02}\text{Mg}_{0.02}\text{Mo}_{0.02}\text{Nb}_{0.01}\text{O}_2$ , HE-N60 with the composition of  $\text{LiNi}_{0.6}\text{Mn}_{0.33}\text{Ti}_{0.02}\text{Mg}_{0.02}\text{Mo}_{0.02}\text{Nb}_{0.01}\text{O}_2$ , and AZCV-LNMO with the composition of  $\text{LiNi}_{0.8}\text{Mn}_{0.13}\text{Al}_{0.02}\text{Zr}_{0.02}\text{Cr}_{0.02}\text{V}_{0.01}\text{O}_2$  are synthesized using a similar co-precipitation method. Electrochemical and X-ray experiments show that all cathodes deliver reduced strain and improved capacity retention and bulk/surface structural stability. Although these experimental-stage cathode materials are far from optimized, the results confirm that the

compositionally complex doping strategy is universally applicable in all zero-Co cathode materials.

In conclusion, a compositionally complex (high-entropy) doping strategy is proposed to fabricate zero-strain high-Ni and zero-Co layered cathodes with superior structural, thermal and mechanical stabilities and long cycle life. The volumetric strain of the high-Ni cathode during operation is pushed down to a 0.3%, far below the critical value of zero strain (1%). The significantly reduced lattice strain leads to an ultra-stable lattice structure that can effectively resist chemo-mechanical cracking as well as lattice defects during long-term

cycling. Owing to the pinning effects of the dopants, the oxygen loss and the detrimental rock-salt transformation are considerably mitigated, leading to superior structural stability in both harsh long-term chemo-mechanical cycle conditions and thermal abuse conditions. The cathode chemistries demonstrated here open up the possibility of optimizing all intercalation electrodes through a dilute multicomponent effect. We expect that this high-entropy doping strategy will guide the design and deployment of safe, long-life, high-energy-density electrodes for next-generation LIBs and other rechargeable batteries.

## Online content

Any methods, additional references, Nature Research reporting summaries, source data, extended data, supplementary information, acknowledgements, peer review information; details of author contributions and competing interests; and statements of data and code availability are available at <https://doi.org/10.1038/s41586-022-05115-z>.

1. Turcheniuk, K., Bondarev, D., Singhal, V. & Yushin, G. Ten years left to redesign lithium-ion batteries. *Nature* **559**, 467–470 (2018).
2. Li, W., Erickson, E. M. & Manthiram, A. High-nickel layered oxide cathodes for lithium-based automotive batteries. *Nat. Energy* **5**, 26–34 (2020).
3. Li, W., Lee, S. & Manthiram, A. High-nickel NMA: a cobalt-free alternative to NMC and NCA cathodes for lithium-ion batteries. *Adv. Mater.* **32**, 2002718 (2020).
4. Bi, Y. et al. Reversible planar gliding and microcracking in a single-crystalline Ni-rich cathode. *Science* **370**, 1313–1317 (2020).
5. Liu, H. et al. A disordered rock salt anode for fast-charging lithium-ion batteries. *Nature* **585**, 63–67 (2020).
6. Lin, R. et al. Anomalous metal segregation in lithium-rich material provides design rules for stable cathode in lithium-ion battery. *Nat. Commun.* **10**, 1650 (2019).
7. Manthiram, A. & Goodenough, J. B. Layered lithium cobalt oxide cathodes. *Nat. Energy* **6**, 323–323 (2021).
8. Liu, W. et al. Nickel-rich layered lithium transition-metal oxide for high-energy lithium-ion batteries. *Angew. Chem. Int. Edn Engl.* **54**, 4440–4457 (2015).
9. Yan, P. et al. Coupling of electrochemically triggered thermal and mechanical effects to aggravate failure in a layered cathode. *Nat. Commun.* **9**, 2437 (2018).
10. Yan, P. et al. Tailoring grain boundary structures and chemistry of Ni-rich layered cathodes for enhanced cycle stability of lithium-ion batteries. *Nat. Energy* **3**, 600–605 (2018).
11. Bianchini, M., Roca-Ayats, M., Hartmann, P., Brezesinski, T. & Janek, J. There and back again—the journey of  $\text{LiNiO}_2$  as a cathode active material. *Angew. Chem. Int. Edn Engl.* **58**, 10434–10458 (2019).
12. Manthiram, A. A reflection on lithium-ion battery cathode chemistry. *Nat. Commun.* **11**, 1550 (2020).
13. Liu, T. et al. Understanding Co roles towards developing Co-free Ni-rich cathodes for rechargeable batteries. *Nat. Energy* **6**, 277–286 (2021).
14. Li, J. et al. Structural origin of the high-voltage instability of lithium cobalt oxide. *Nat. Nanotechnol.* **16**, 599–605 (2021).
15. Mu, L. et al. Dopant distribution in Co-free high-energy layered cathode materials. *Chem. Mater.* **31**, 9769–9776 (2019).
16. Mu, L. et al. Structural and electrochemical impacts of Mg/Mn dual dopants on the  $\text{LiNiO}_2$  cathode in Li-metal batteries. *ACS Appl. Mater. Interfaces* **12**, 12874–12882 (2020).
17. Sun, H. H. et al. Beyond doping and coating: prospective strategies for stable high-capacity layered Ni-rich cathodes. *ACS Energy Lett.* **5**, 1136–1146 (2020).
18. Xie, Q., Li, W. & Manthiram, A. A Mg-doped high-nickel layered oxide cathode enabling safer, high-energy-density Li-ion batteries. *Chem. Mater.* **31**, 938–946 (2019).
19. Wang, C. et al. Resolving atomic-scale phase transformation and oxygen loss mechanism in ultrahigh-nickel layered cathodes for cobalt-free lithium-ion batteries. *Matter* **4**, 2013–2026 (2021).
20. Wang, C., Zhang, R., Kisslinger, K. & Xin, H. L. Atomic-scale observation of O1 faulted phase-induced deactivation of  $\text{LiNiO}_2$  at high voltage. *Nano Lett.* **21**, 3657–3663 (2021).
21. Feng, X., Ren, D., He, X. & Ouyang, M. Mitigating thermal runaway of lithium-ion batteries. *Joule* **4**, 743–770 (2020).
22. Yan, P. et al. Intragranular cracking as a critical barrier for high-voltage usage of layer-structured cathode for lithium-ion batteries. *Nat. Commun.* **8**, 14101 (2017).
23. Zeng, X., Zhan, C., Lu, J. & Amine, K. Stabilization of a High-capacity and high-power nickel-based cathode for Li-ion batteries. *Chem* **4**, 690–704 (2018).
24. Huang, Y. et al. Thermal stability and reactivity of cathode materials for Li-ion batteries. *ACS Appl. Mater. Interfaces* **8**, 7013–7021 (2016).
25. Yeh, J. W. et al. Nanostructured high-entropy alloys with multiple principal elements: novel alloy design concepts and outcomes. *Adv. Eng. Mater.* **6**, 299–303 (2004).
26. Zhao, C., Ding, F., Lu, Y., Chen, L. & Hu, Y. S. High-entropy layered oxide cathodes for sodium-ion batteries. *Angew. Chem. Int. Edn Engl.* **59**, 264–269 (2020).
27. Lun, Z. et al. Cation-disordered rocksalt-type high-entropy cathodes for Li-ion batteries. *Nat. Mater.* **20**, 214–221 (2021).
28. Wang, J. et al. Lithium containing layered high entropy oxide structures. *Sci. Rep.* **10**, 18430 (2020).
29. Zou, L. et al. Lattice doping regulated interfacial reactions in cathode for enhanced cycling stability. *Nat. Commun.* **10**, 3447 (2019).
30. Bak, S.-M. et al. Structural changes and thermal stability of charged  $\text{LiNi}_x\text{Mn}_{1-x}\text{Co}_2\text{O}_2$  cathode materials studied by combined in situ time-resolved XRD and mass spectroscopy. *ACS Appl. Mater. Interfaces* **6**, 22594–22601 (2014).
31. Yoon, M. et al. Reactive boride infusion stabilizes Ni-rich cathodes for lithium-ion batteries. *Nat. Energy* **6**, 362–371 (2021).
32. Xu, J. et al. Understanding the degradation mechanism of lithium nickel oxide cathodes for Li-ion batteries. *ACS Appl. Mater. Interfaces* **8**, 31677–31683 (2016).
33. Tian, C. et al. Charge heterogeneity and surface chemistry in polycrystalline cathode materials. *Joule* **2**, 464–477 (2018).
34. Ohzuku, T., Ueda, A. & Yamamoto, N. Zero-strain insertion material of  $\text{Li}[\text{Li}^{1/3}\text{Ti}^{5/3}]^{\text{O}}_4$  for rechargeable lithium cells. *J. Electrochem. Soc.* **142**, 1431 (1995).

**Publisher's note** Springer Nature remains neutral with regard to jurisdictional claims in published maps and institutional affiliations.

Springer Nature or its licensor holds exclusive rights to this article under a publishing agreement with the author(s) or other rightsholder(s); author self-archiving of the accepted manuscript version of this article is solely governed by the terms of such publishing agreement and applicable law.

© The Author(s), under exclusive licence to Springer Nature Limited 2022

## Methods

### Materials synthesis

HE-LNMO is synthesized using a co-precipitation method in water solution. Hydroxide precursor with stoichiometric ratio  $\text{Ni}_{0.8}\text{Mn}_{0.13}\text{Ti}_{0.02}\text{Mg}_{0.02}\text{Nb}_{0.01}\text{Mo}_{0.02}(\text{OH})_2$  is synthesized. First,  $\text{NiSO}_4 \cdot 6\text{H}_2\text{O}$  (99.8%, Fisher),  $\text{MnSO}_4 \cdot 4\text{H}_2\text{O}$  (99%, Fisher),  $\text{MgSO}_4 \cdot 7\text{H}_2\text{O}$  (98%, ACROS),  $\text{TiOSO}_4$  solution (Sigma-Aldrich),  $\text{Nb}(\text{HC}_2\text{O}_4)_5$  (Alfa-Aesar) and  $(\text{NH}_4)_6\text{Mo}_7\text{O}_{24}$  (99.98%, Sigma-Aldrich) are dissolved in pure water with a total transition metal concentration of 1 M. The transition metal solution is mixed uniformly using magnetic stirring for 12 h and stored in an Ar-filled bottle. Then, the base solution with 2 M  $\text{NaOH}$  and 1.67 M  $\text{NH}_4\text{OH}$  is mixed and prepared before the reaction. Next, 30 ml of the as-prepared base solution is used as the starting solution. Then, the pH of the starting solution is adjusted to 11.0 by using diluted sulfuric acid, and then the reaction is started by injecting both the transition metal solution and base solution simultaneously with a flow of around 4 ml min<sup>-1</sup>. The product is synthesized by stirring the solution at  $\text{pH} = 11.0 \pm 0.2$ , 60 °C under Ar protection. The laurel-green precipitate is collected using vacuum filtration and washed with pure water to remove the residual ions, and then dried in a vacuum oven at 110 °C. Second, the dried transition metal hydroxide precursor powder is mixed thoroughly with LiOH powder with 5% excess Li as compensation at high temperatures. The HE-LNMO precursor is calcined in a tube furnace at 730 °C for 12 h under an oxygen flow of 0.5 l min<sup>-1</sup>.

The NMC-811 cathode material used in this work is a commercial material (Targray, product SNMC03004, lot no. 12846), provided by the Cell Analysis, Modeling, and Prototyping (CAMP) Facility at Argonne National Laboratory. The graphite anode material is commercial Superior Graphite SLC1520P (lot no. 022626-551) provided by CAMP.

### Electrochemical tests

The electrochemical performances are tested in the CR-2032 coin cell. First, the cathode slurry is prepared by uniformly mixing the active material, super P carbon and 5% polyvinylidene fluoride in *N*-methyl-1,2-pyrrolidone solvent at a mass ratio of 8:1:1. Second, the well-mixed slurry is coated on Al foil and dried in a vacuum oven overnight at 105 °C. The electrode is cut into discs with a diameter of 12 mm, and the mass loading of active material is 2–3 mg cm<sup>-2</sup> for the half-cell test and approximately 8.5 mg cm<sup>-2</sup> for the full-cell test. Finally, the coin cell is assembled in the Ar glovebox using a Li chip (diameter = 16.7 mm) as a counter electrode and Celgard-2025 as the separator. The electrolyte is 1 M  $\text{LiPF}_6$  dissolved in ethylene carbonate: ethyl methyl carbonate = 3:7 solvent with 2 wt% vinylene carbonate as an additive. In the full-cell test, the counter electrode is replaced by commercial graphite coated on copper foil. In the single-layer pouch cell test, the cathode areal capacity is around 1.8 mAh cm<sup>-2</sup>, and the cathode size is slightly smaller than the anode size. The electrochemical performance is conducted on a NEWARE BTS-4000 battery test system at room temperature (25 °C). The test voltage is 2.5–4.4 V, and the current rate ranges from 0.1C to 2C. The GITT is carried out using a typical step profile at 0.1C with 20 min pulse current and 5 min rest. CV and EIS tests are conducted on a BioLogic VMP-3 workstation, and CV is tested from 2.5 to 4.5 V at 0.1 mV s<sup>-1</sup> scanning speed.

### TEM experiments

To prepare the TEM sample, the cells are disassembled, and the electrodes are washed with dimethyl carbonate (DMC) and dried in an Ar-filled glovebox. The electrodes are ultrasonicated in DMC and dispersed on the grid in a glovebox. The (S)TEM experiments are performed on a transmission electron microscope with a field emission source operated at 200 keV. The atomic-resolution annular dark-field imaging is performed in HAADF-STEM mode. Energy-dispersive X-ray spectroscopy (EDS) analysis is performed with Super-X EDS detectors integrated into the TEM. The in-situ delithiation experiments are conducted with a Nanofactory STM-TEM holder.

### X-ray techniques

The hard X-ray absorption spectroscopy of transition metal ions is performed on the 7-BM QAS beamline 7-BM at National Synchrotron Light Source II (NSLS II), Brookhaven National Laboratory. The corresponding X-ray absorption data are analysed by Athena software and the wavelet-transformed (WT)-EXAFS is analysed using HAMA code developed by H. Funke and M. Chukalina<sup>35</sup>. To prepare the sample, the corresponding cells are disassembled, and the electrodes are washed with DMC and dried in an Ar-filled glovebox. The electrodes are sealed by Kapton tape to avoid air exposure. TXM experiments are conducted at beamline 18-ID FXI at NSLS II, which offers advanced capabilities for studying the morphology and oxidation states of dynamic systems in two and three dimensions with 30 nm resolution. Sample preparation for TXM experiments is similar to that of hard X-ray experiments, whereas the active material loading is lower to avoid the overlap of particles. X-ray fluorescence mapping is performed at the 5-ID SRX beamline at NSLS II. Fluorescence spectra are collected with a seven-element silicon drift detector (SSD). A series of X-ray thin films is scanned as XRF calibration standards (Micromatter Technologies Inc.). Data are fitted and quantified using the open-source software PyXRF<sup>36</sup>. The soft X-ray absorption including the TEY and FY modes is performed at beamline 10-1 at the Stanford Synchrotron Radiation Lightsource, and the energy shift is calibrated by the transition metal foil. Samples are prepared in a glovebox and transferred immediately to the vacuum chamber. The in-situ heating and charge–discharge XRD and ex-situ XRD are performed on beamline 11-ID-C at the Advanced Photon Source. The beamline is optimized for high-energy XRD at 105.7 keV. For the in-situ heating, a charged electrode including the current collector (cutoff at 4.4 V versus  $\text{Li}/\text{Li}^+$ ) is sealed by Kapton tape and fixed on the heating holder. For the in-situ charge and discharge, the in-situ cell with 2 mm windows on both the positive and negative cell cases is prepared; for the ex-situ test, the electrode is washed and dried in the glovebox and then scraped down by a blade. The powder is then transferred into a 1 mm Kapton tube and sealed with wax. The diffraction patterns are recorded with the beam passing through the electrode. All the XRD data are calibrated and analysed by GSAS-II software.

### DSC/TGA test

All the DSC/TGA samples are charged to 4.4 V (versus  $\text{Li}/\text{Li}^+$ ) and disassembled in a glovebox. The heating rate for the test is 10 °C min<sup>-1</sup>. For the DSC test, TA instrument DSC Q2000 equipped with an air-fin cooler is applied, providing temperature measurements of material phase transitions. NETZSCH STA 449 F3 Jupiter is applied for the TGA–MS test, enabling the measurement of temperature and oxygen loss during the phase transformation.

### Strain, capacity and Ni content data

Some of the strain, capacity and Ni content data such as  $\text{LiVO}_2$ ,  $\text{LiCoO}_2$ , NMC and so on are directly obtained or calculated from additional references<sup>3,37–47</sup>.

### Data availability

Source data are provided with this paper. The data that support the findings of this study are available from the corresponding author (huolin.xin@uci.edu) upon reasonable request.

35. Funke, H., Scheinost, A. C. & Chukalina, M. Wavelet analysis of extended x-ray absorption fine structure data. *Phys. Rev. B* **71**, 094110 (2005).
36. Li, L. et al. In *X-Ray Nanoimaging: Instruments and Methods III* vol. 10389 (eds Somogyi, A. & Lai, B.) <https://doi.org/10.1117/12.2272585> (Proc. SPIE, International Society for Optical Engineering, 2017).
37. Sun, X. et al. New phases and phase transitions observed in over-charged states of  $\text{LiCoO}_2$ -based cathode materials. *J. Power Sources* **97–98**, 274–276 (2001).
38. de Picciotto, L. A., Thackeray, M. M., David, W. I. F., Bruce, P. G. & Goodenough, J. B. Structural characterization of delithiated  $\text{LiVO}_2$ . *Mater. Res. Bull.* **19**, 1497–1506 (1984).

39. Zhou, Y.-N. et al. Tuning charge–discharge induced unit cell breathing in layer-structured cathode materials for lithium-ion batteries. *Nat. Commun.* **5**, 5381 (2014).
40. Liu, H. et al. Intergranular cracking as a major cause of long-term capacity fading of layered cathodes. *Nano Lett.* **17**, 3452–3457 (2017).
41. Watanabe, S., Kinoshita, M., Hosokawa, T., Morigaki, K. & Nakura, K. Capacity fading of  $\text{LiAl}_{1-x-y}\text{Ni}_{x}\text{Co}_{y}\text{O}_2$  cathode for lithium-ion batteries during accelerated calendar and cycle life tests (effect of depth of discharge in charge–discharge cycling on the suppression of the micro-crack generation of  $\text{LiAl}_{1-x-y}\text{Ni}_{x}\text{Co}_{y}\text{O}_2$  particle). *J. Power Sources* **260**, 50–56 (2014).
42. de Biasi, L. et al. Between scylla and charybdis: balancing among structural stability and energy density of layered NCM cathode materials for advanced lithium-ion batteries. *J. Phys. Chem. C* **121**, 26163–26171 (2017).
43. Cui, Z., Xie, Q. & Manthiram, A. Zinc-doped high-nickel, low-cobalt layered oxide cathodes for high-energy-density lithium-ion batteries. *ACS Appl. Mater. Interfaces* **13**, 15324–15332 (2021).
44. Lee, S. et al. In-depth analysis of the degradation mechanisms of high-nickel, low/no-cobalt layered oxide cathodes for lithium-ion batteries. *Adv. Energy Mater.* **11**, 2100858 (2021).
45. Xie, Q., Cui, Z. & Manthiram, A. Unveiling the stabilities of nickel-based layered oxide cathodes at an identical degree of delithiation in lithium-based batteries. *Adv. Mater.* **33**, 2100804 (2021).
46. Zhou, K., Xie, Q., Li, B. & Manthiram, A. An in-depth understanding of the effect of aluminum doping in high-nickel cathodes for lithium-ion batteries. *Energy Storage Mater.* **34**, 229–240 (2021).
47. Yoon, C. S. et al. High-energy Ni-rich  $\text{Li}[\text{Ni}_x\text{Co}_y\text{Mn}_{1-x-y}]\text{O}_2$  cathodes via compositional partitioning for next-generation electric vehicles. *Chem. Mater.* **29**, 10436–10445 (2017).

**Acknowledgements** This work is primarily supported by the US Department of Energy (DOE)'s Office of Energy Efficiency and Renewable Energy (EERE) under award no. DE-EE0008444. The in situ TEM study of Li deintercalation is supported by US DOE's Office of Basic Energy Sciences, under award no. DE-SC0021204. The work done by R.Z. for this study was funded by the startup funding of H.L.X. R.L. was supported by the Assistant Secretary for EERE, Vehicle Technology Office of the US DOE through the Advanced Battery Materials Research (BMR) Program, under contract no. DE-SC0012704. The work performed at Pacific Northwest National Laboratory was supported by the US DOE's Office of EERE through the Applied Battery Research Program under contract no. DE-AC05-76RL01830. This research used the

resources of the Center for Functional Nanomaterials as well as 7-BM, 18-ID, 5-ID beamlines of the National Synchrotron Light Source II, which are two US DOE Office of Science facilities, at Brookhaven National Laboratory under contract no. DE-SC0012704. This research used the resources of the Advanced Photon Source, a US DOE Office of Science User Facility operated for the DOE Office of Science by Argonne National Laboratory under contract no. DE-AC02-06CH11357. Use of the Stanford Synchrotron Radiation Lightsource, SLAC National Accelerator Laboratory, is supported by the US DOE, Office of Science, Office of Basic Energy Sciences under contract no. DE-AC02-76SF00515. We acknowledge the use of facilities and instrumentation at the UC Irvine Materials Research Institute, which is supported in part by the National Science Foundation through the UC Irvine Materials Research Science and Engineering Center (no. DMR-2011967). We also acknowledge the electrode produced at the US DOE's Cell Analysis, Modeling, and Prototyping (CAMP) Facility, Argonne National Laboratory. The CAMP Facility is fully supported by the DOE Vehicle Technologies Office.

**Author contributions** H.L.X. conceived the idea and directed the project. R.Z. synthesized the materials and performed the electrochemical experiments, soft/hard XAS experiments and data analysis. C.W. performed the in-situ and ex-situ TEM experiments and analyses, and TXM tomography data analyses. P.Z. performed the DSC and TGA-MS experiments. Y.R., L.Y., T.L. and Wenqian Xu performed in-situ and ex-situ XRD experiments. R.L., S.N.E. and L.M. performed the XANES and EXAFS measurements. H.J., Q.L. and Wu Xu prepared electrolytes and helped with the single-layer pouch cell test. M.G. performed the TXM experiments and data analysis. Y.Y. and A.M.K. performed the X-ray fluorescence experiments. S.S. and S.J.L. performed the soft X-ray absorption experiment. K.K. performed the FIB-SEM experiments. B.P. and S.T. fabricated the commercial NMC cathode. C.W., R.Z. and H.L.X. wrote the paper with the help of all authors.

**Competing interests** H.L.X. reports two US non-provisional patent applications and a PCT application filed by the University of California, Irvine, on the basis of this work.

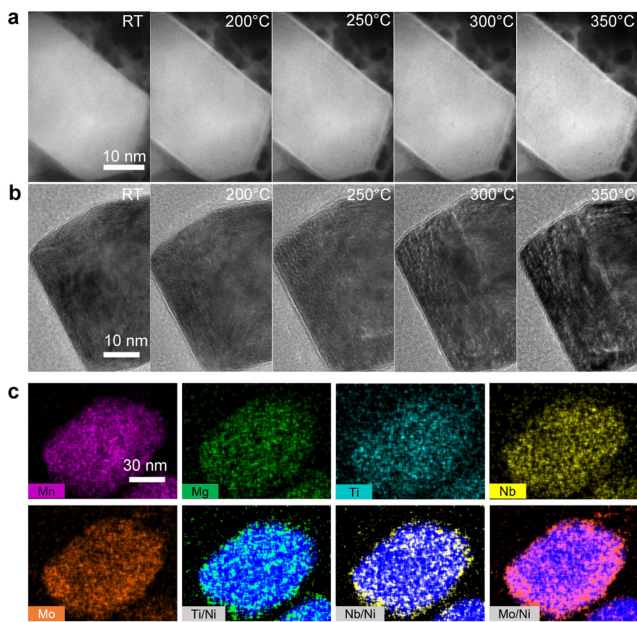
#### Additional information

**Supplementary information** The online version contains supplementary material available at <https://doi.org/10.1038/s41586-022-05115-z>.

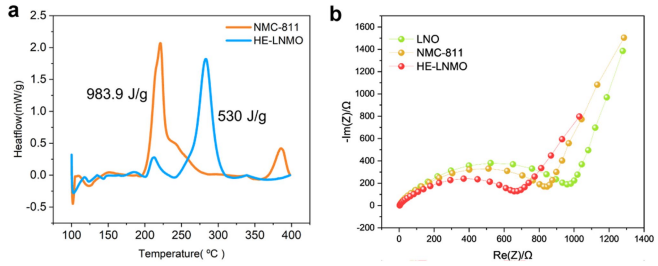
**Correspondence and requests for materials** should be addressed to Huolin L. Xin.

**Peer review information** *Nature* thanks the anonymous reviewers for their contribution to the peer review of this work.

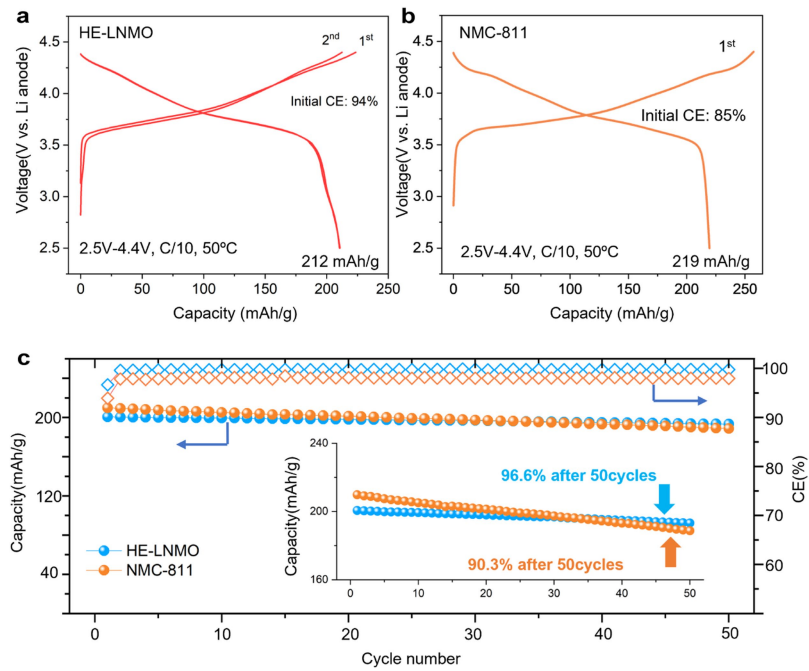
**Reprints and permissions information** is available at <http://www.nature.com/reprints>.

**Extended Data Fig. 1 | In-situ heating low-mag S/TEM and EDS mapping.**

**a**, In-situ heating HAADF-STEM of charged HE-LNMO up to 350 °C. **b**, In-situ heating TEM of charged NMC-811 up to 350 °C. **c**, EDS mapping of charged HE-LNMO after heating at 350 °C.

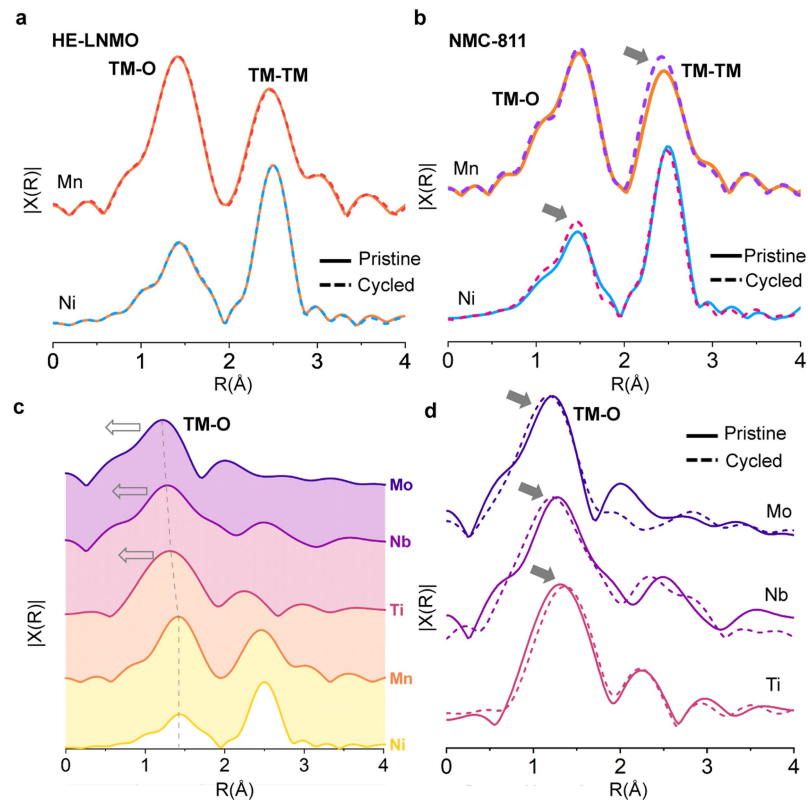


**Extended Data Fig. 2 | Thermal stability and impedance of NMC-811 and HE-LNMO.** **a**, Quantified DSC result of charged state NMC-811 and HE-LNMO. Both electrodes are CC+CV charged to 4.4 V at 0.1 C current. **b**, EIS of LNO, NMC-811, and HE-LNMO under the same cell condition. The result shows that HE-LNMO has the lowest impedance and pure LNO has the largest impedance.



**Extended Data Fig. 3 | High-temperature cycling performance of NMC-811 and HE-LNMO.** **a–b**, Galvanostatic charge/discharge curve of HE-LNMO and NMC-811 at 50 °C, C/10. The result shows the initial Columbic efficiency of

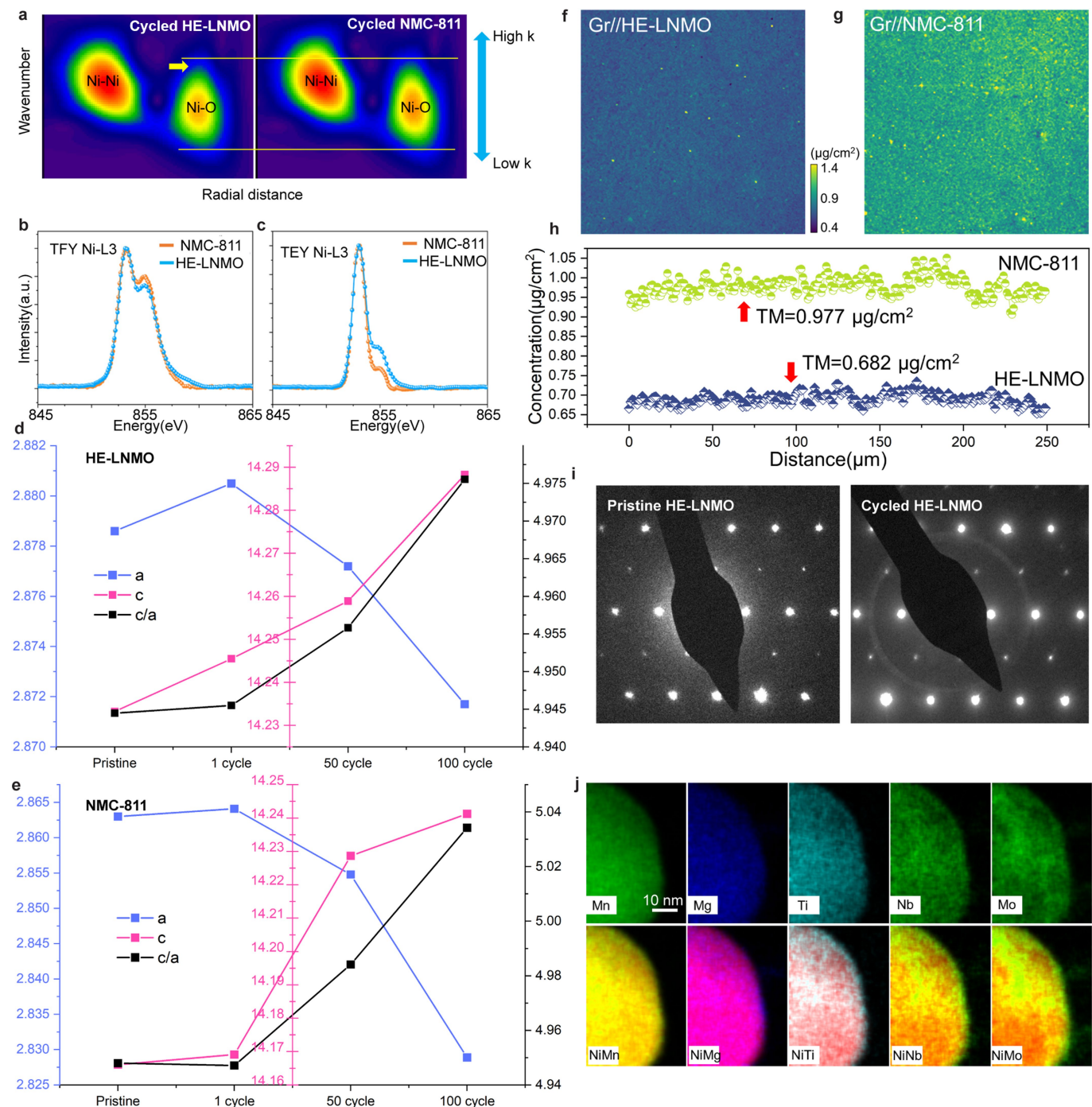
HE-LNMO (94%) is significantly higher than that of the NMC-811 (85%), indicating much less side reaction in HE-LNMO compared with NMC-811. **c**, cycling performance of HE-LNMO and NMC-811 at 50 °C, C/2.



**Extended Data Fig. 4 | FT-EXAFS of transition metals in HE-LNMO and NMC-811 before and after cycling.** **a–b**, FT-EXAFS of Ni, Mn before and after cycling. The TM-O bonding and TM-TM coordinate in (a) HE-LNMO and (b)

NMC-811, respectively. **c**, FT-EXAFS of Ni, Mn, Ti, Nb and Mo in pristine HE-LNMO. **d**, FT-EXAFS of Ti, Nb and Mo in pristine and cycled HE-LNMO.

# Article



**Extended Data Fig. 5 | Multi-dimensional structural-stability characterization of NMC-811 and HE-LNMO.** **a**, Wavelet-transformed Ni-K edge EXAFS of HE-LNMO and NMC-811 during long-term cycling. **b–c**, Soft X-ray absorption (XAS) of Ni-L3 edge in cycled NMC-811 and HE-LNMO (cutoff 2.5–4.3 V, 1C) at TFY mode (**b**) and TEY mode (**c**). **d–e**, Lattice parameters change during long cycling of (**d**) HE-LNMO and (**e**) NMC-811 calculated by XRD. **f–h**, X-ray fluorescence (XRF) mapping result of Ni dissolution on the graphite

(Gr) anode. Ni distribution on Gr anode paired with HE-LNMO (**f**) and NMC-811 (**g**), respectively (cycling condition: 2.5V–4.4 V vs Gr, 1C; field of view: 0.25mm\*0.25mm). **h**, Quantitative result derived from the data in **f** and **g**.

**i**, SAED pattern of pristine HE-LNMO cathode and that after 500th long cycles.

**j**, EDS mapping of long cycled HE-LNMO, showing the stable element distribution during long cycling.

**Extended Data Table 1 | Capacity vs. Volume change in the state-of-art high-Ni, low-Co and benchmark cathodes**

Cathode	Capacity (mAh/g)	$\Delta V\%$	Retention(100 cycles)	Ref
<b>LiNiO<sub>2</sub></b>	~225	-8.1	74% (2.8-4.4V, C/3)	Ref(43)
LiNi <sub>0.94</sub> Co <sub>0.04</sub> Zn <sub>0.02</sub> O <sub>1.99</sub>	~225	-6.3(4.3V)	86.7%(2.8-4.4V, C/3)	Ref(41)
LiNi <sub>0.94</sub> Co <sub>0.06</sub> O <sub>2</sub>	~232	-7.3(4.3V)	74.7%(2.8-4.4V, C/3)	Ref(41)
LiNi <sub>0.89</sub> Mn <sub>0.055</sub> Co <sub>0.055</sub> O <sub>2</sub>	~225	-5.1(4.3V)	91%(2.8-4.4V, C/3)	Ref(42)
<b>LiNi<sub>0.883</sub>Mn<sub>0.056</sub>Al<sub>0.061</sub>O<sub>2</sub></b>	~211	-2.6(4.3V)	90%(2.8-4.4V, C/3)	Ref(3)
LiNi <sub>0.89</sub> Mn <sub>0.044</sub> Co <sub>0.042</sub> Al <sub>0.013</sub> Mg <sub>0.011</sub> O <sub>2</sub>	~212	-4.0(4.3V)	93%(2.8-4.4V, C/3)	Ref(44)
LiNi <sub>0.85</sub> Co <sub>0.054</sub> Al <sub>0.096</sub> O <sub>2</sub>	~175	-5.8(4.3V)	89%(2.8-4.4V, C/3)	Ref(44)
<b>LiNi<sub>0.85</sub>Al<sub>0.15</sub>O<sub>2</sub></b>	~172	-7.2	~92%(2.8-4.4V, C/3)	Ref(44)
Li <sub>1.02</sub> Ni <sub>0.85</sub> Co <sub>0.1</sub> Mn <sub>0.05</sub> O <sub>2</sub>	~215	-6.0(4.3V)	(Not available)	Ref(40)
LiNi <sub>0.8</sub> Co <sub>0.1</sub> Mn <sub>0.1</sub> O <sub>2</sub>	~210	-5.5(4.3V)	87%(2.5-4.4V, C/3)	Ref(43)
<b>HE-LNMO (this work)</b>	~205	-0.3(4.3V)	98.5%(2.5-4.4V, C/3)	
LiNi <sub>0.9</sub> Co <sub>0.05</sub> Mn <sub>0.05</sub> O <sub>2</sub>	~220		~77%(2.5-4.3V, C/3)	Ref(45)
LiNi <sub>0.6</sub> Co <sub>0.2</sub> Mn <sub>0.2</sub> O <sub>2</sub>	~203	-2.5(4.3V)	~92%(2.5-4.3V, C/3)	Ref(40,45)
LiNi <sub>0.5</sub> Co <sub>0.2</sub> Mn <sub>0.3</sub> O <sub>2</sub>	~190	-1.8(4.3V)	~96%(2.5-4.3V, C/3)	Ref(40,45)
LiNi <sub>0.33</sub> Co <sub>0.33</sub> Mn <sub>0.33</sub> O <sub>2</sub>	~187		~97.5%(2.5-4.3V, C/3)	Ref(40,45)

Summaries of discharge capacity, volume change and capacity retention in state-of-art high-Ni, low-Co/zero-Co cathode materials. Zero-Co cathodes are labeled as bold. Volume change is calculated based on the lattice parameters *a* and *c*.